University of Amsterdam

Coherent anti-Stokes Raman scattering microscopy for quantitative characterization of mixing and flow in microfluidics

Schafer, D.; Müller, M.; Bonn, M.; Marr, D.W.M.; van Maarseveen, J.; Squier, J.

Link to publication

Coherent anti-Stokes Raman scattering microscopy for quantitative characterization of mixing and flow in microfluidics

Dawn Schafer,[1,]* Michiel Müller,[2] Mischa Bonn,[3] David W. M. Marr,[4] Jan van Maarseveen,[5] and Jeff Squier[1]

[1]*Department of Physics, Colorado School of Mines, 1523 Illinois Street, Golden, Colorado 80401, USA*
[2]*Swammerdam Institute for Life Sciences, University of Amsterdam, P.O. Box 94062,*
1090 GB Amsterdam, The Netherlands
[3]*FOM Institute for Atomic and Molecular Physics (AMOLF), Kruislaan 407, Amsterdam, The Netherlands*
[4]*Department of Chemical Engineering, Colorado School of Mines, 1523 Illinois Street, Golden, Colorado 80401, USA*
[5]*Van 't Hoff Institute for Molecular Sciences, University of Amsterdam, Nieuwe Achtergracht 129,*
1018 WS Amsterdam, The Netherlands
*Corresponding author: dschafer@mines.edu

We present an optical, noninvasive and label-free approach to characterize flow profiles in microfluidic devices. Coherent anti-Stokes Raman scattering signals were used to map the mass transport in a microfluidic device that was then related back to the local flow rate of dilute solutes having constant fluid properties. Flow characterization was demonstrated in two common types of microfluidic devices, polydimethylsiloxane/ glass square channels and wet-etched glass tapered channels. © 2009 Optical Society of America
OCIS codes: 300.6230, 180.4315.

Engineered microfluidic systems have enhanced biological and chemical analysis by enabling the high throughput screening of thermal and chemical parameters [1,2] and the study of rapid mixing and flow conditions, which have revealed microsecond reaction events [3] and nanosecond structural changes [4]. Building on this success, microfluidic devices with integrated Raman microscopy have shown they can monitor thermal and chemical gradients, product formation, and conformational changes [4–9]. Within such devices, optical resolution of molecular kinetics is limited more by the optical sectioning than by the stability of the conditions within the microfluidic device. In these applications, coherent anti-Stokes Raman scattering (CARS), a nonlinear Raman microscopy, is a particularly attractive alternative by virtue of its improved spatial and temporal resolution. We have previously demonstrated *in situ* quantitative CARS imaging of product formation inside a microfluidic device with submicrometer lateral resolution and ~millimolar sensitivity on a millisecond time scale [9]. Here, we use high-resolution mass transport measurements in microfluidic devices using CARS to infer the local flow profile, providing the necessary device characterization for subsequent studies on concentration- or time-dependent molecular dynamics.

Imaging local concentration or flow profiles has been demonstrated by fluorescence-based techniques, including particle image velocimetry and scalar fluorescence studies [10,11], light microscopy [12], confocal fluorescence microscopy [13], and multiphoton microscopy [14]. However, to follow untagged molecules, especially rapid diffusers—small molecules that typically do not fluoresce—an alternative Raman-based approach is attractive, directly quantifying local concentration with high chemical specificity by making use of inherent molecular vibrations of molecules. Tracking mixing in reagent-limited studies by spontaneous Raman analyses may be hindered owing to the long integration times required (seconds to minutes) [15,16]. By employing the stimulated Raman technique CARS, rapid data collection is feasible, allowing the local flow rate to be determined by taking advantage of the simple mass transport behavior associated with typical microfluidic flows. We quantify the mass transport and local flow rates in two microfluidic arrangements: an all-glass system and a polydimethylsiloxane (PDMS) device sealed to glass.

On the small length scales characteristic of microfluidic channels, flow is typically laminar and mixing is dominated by diffusion. In such systems the fluid dynamics for incompressible Newtonian fluids are well described by the Navier–Stokes equations that, for dilute fluids having constant density, viscosity, and diffusion coefficient, can be solved independently of the mass transport to provide the velocity profile in the channel. To subsequently determine the mass distribution of a dilute solute, the calculated velocity profile can be inserted into Fick's law. For systems without velocity gradients, however, the solution is dictated by diffusion alone; for example, in simple 1D diffusion with an initial stepwise concentration profile the analytical solution is given by

$$\frac{C(y,t)}{C_0} = \frac{1}{2}\left\{1 + \mathrm{erf}\left[\frac{-y}{w(t)}\right]\right\}, \qquad (1)$$

where C is the local concentration weighted by the initial concentration C_0 and w is the width of the diffusion profile normal to the flow (y direction) with the orientation of the microfluidic shown in Fig. 1(a). The width of the diffusion profile evolves in time as $w(t) = (4Dx/v)^{1/2}$, where D is the diffusion coefficient, x is
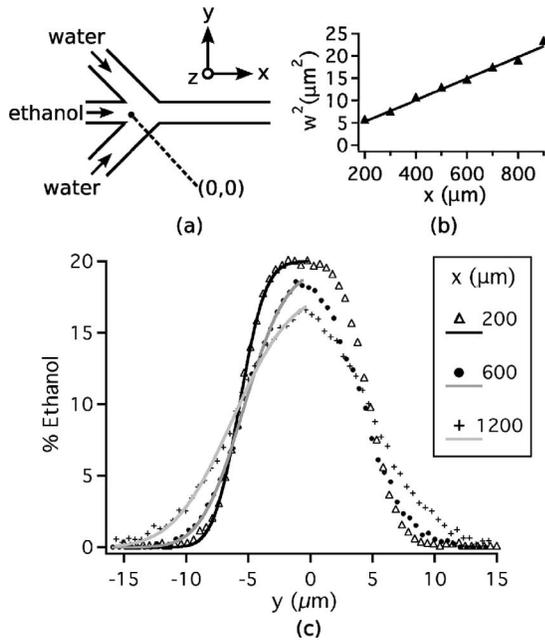
Fig. 1.   Sample data set for the etched glass microfluidic. (a) Orientation of the three-inlet mixing geometry; (b) the relation between the width squared, w^2, of the diffusion profile in y and the downstream position, x; (c) ethanol concentration line outs in y for several positions, x.
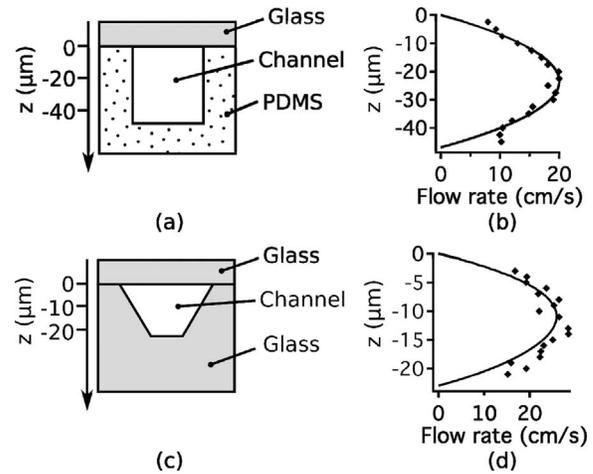

Fig. 2.   (a) Illustration of the channel cross section for the PDMS/glass microfluidic and (b) the maximum local flow rate as a function of depth (z) where the solid curve is a simulation. (c) Illustration of the channel cross section for the etched glass microfluidic and (d) the maximum local flow rate as a function of depth where the solid curve is a simulation.

the coordinate parallel to flow, and v is the flow rate. Although the expected velocity profile in pressure-driven flow is parabolic in y, approaching zero at the walls, the flow rate varies little within the central region near the maximum of the parabola. In addition, the velocity is independent of x in uniform channels, allowing Eq. (1) to be applied to mass transport in our microfluidics. In our experiments w was calculated by fitting the measured concentration profile in the y direction to Eq. (1). The relationship between w and x was determined by repeating the measurement at several x positions. Using these data and assuming a known and constant diffusion coefficient, the local flow rate, v, was calculated. Finally, the dependence of flow rate on depth (z) was determined by repeating the measurements at multiple depths.

For quantitative flow analysis, we measured the mass transport of a 20% ethanol solution in deionized water, for which the diffusion coefficient is well known (1.28×10^{-9} m^2/s). From the mass transport measurements we calculated the flow profile along the channel depth in two commonly used microfluidic designs: square channels in PDMS sealed to glass and channels of varying width etched in glass. Etched glass microfluidic devices with a hydrodynamic focusing, three-inlet mixing junction were purchased from Micronit (Enschede, The Netherlands). Channels were 23 μm deep, and the width tapered from 47 μm to 14 μm (top to bottom) as illustrated in Fig. 2(c). The ends of the channel network were connected to holes through the top plate into which fluids were delivered through 160 μm diameter fused-silica capillaries and driven by syringe pumps at flow rates of about 5×10^{-3} mL/min. PDMS/glass microfluidics were constructed using soft-lithography tech-

niques [17] and a template in SU-8 2050 photoresist on a silicon wafer. PDMS was poured onto the template, heat cured, removed, and then chemically bonded to a fused-silica microscope slide after exposure to oxygen plasma, resulting in nearly square channels 50 μm wide and 47 μm deep. In contrast to the commercial-etched glass microfluidics, which are designed for use with a syringe pump, the PDMS devices offered the flexibility to use high-pressure silicone tubing and pressurized reservoirs to achieve comparable flow rates ($\sim 5 \times 10^{-3}$ mL/min).

The experimental setup for multiplex CARS (mCARS) overlaps a 10 ps (bandwidth 1.5 cm^{-1} FWHM) pump–probe laser at 710 nm in time and space with an 80 fs (bandwidth $\sim$180 cm^{-1} FWHM) Stokes laser [18]. The Stokes laser was tunable between 750 and 950 nm, corresponding to a vibrational range of $\sim 750-3500$ cm^{-1}. The laser beams were focused with an oil-immersion objective (1.4 NA) into the microfluidic, providing submicrometer lateral resolution. The axial resolution was measured to be 3.6 μm FWHM. The generated anti-Stokes signal was collected by a second objective (0.4 NA) then filtered and spectrally resolved with an effective resolution of $\sim$5 cm^{-1}. Spectra were collected in the form of line scans perpendicular to flow (y). Each line scan spanned the central 30 μm region of the channel with 60 evenly spaced pixels. Line scans were taken at positions downstream (x) spaced by 100 μm and at depths (z) spaced by $1-2$ μm. The acquisition time per point was 100 ms.

Local ethanol concentration in the device was given by the strength of a vibrational resonance centered at 880 cm^{-1} determined by direct phase retrieval of mCARS spectra using the maximum entropy method (MEM). The MEM was used to extract the linear signal from the imaginary part of the third-order susceptibility of the mCARS signal [19]. A retrieved linear spectrum and its mCARS data are

shown in Fig. 3(a). In Fig. 3(b) the strength of the resonance is shown as a function of ethanol concentration. The concentration of ethanol varied from 0% to 20% across the channel.

A sample measurement set at $z = 8$ μm below the upper wall in the etched glass microfluidic is shown in Fig. 1. Each solid curve on the left-hand side of Fig. 1(c) is the data fit to Eq. (1). For comparison, computational simulations were generated using COMSOL multiphysics finite-element analysis software, solving the steady-state incompressible Navier–Stokes and convection and diffusion partial differential equations for the fluid properties of ethanol in water assuming the no-slip boundary condition at the walls. Fig. 2(a) illustrates the PDMS/glass channel cross section, and Fig. 2(b) shows the calculated local maximum velocity for the measurement (diamonds) and simulation (solid curve). These results show that the experimentally determined velocity profile follows the parabolic prediction to within $3-4$ μm of the channel walls in the z dimension in the imaged region. The results for the etched glass channels are shown in Fig. 2(c) and 2(d). Simulated data matches the measured bulk flow rate of 5.0×10^{-3} mL/min. The nonuniform channel width caused the predicted velocity profile to be slightly asymmetric with the maximum velocity shifted toward the upper boundary. The fluctuations in the velocity for the glass microfluidic in Fig. 2(d), not apparent in the PDMS microfluidic in Fig. 2(b), are likely owing to differences between the two methods used for driving flow.

Flow calibration through high-contrast mass transport measurements in microfluidics is demonstrated using mCARS microscopy. This technique is a useful two-for-one application of mCARS microscopy by providing the prerequisite calibration of the mixing behavior for concentration-dependent molecular kinet-
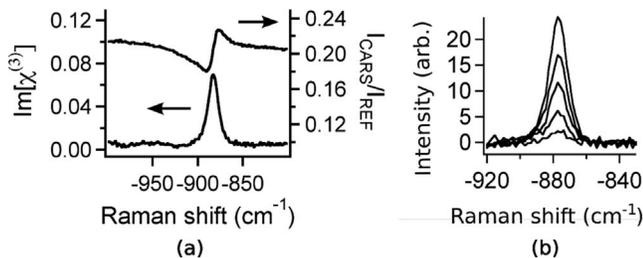
ics studies and of the fluid flow behavior for time-sensitive or shear-sensitive studies. Mass transport in three dimensions is rapidly quantified according to the inherently unique vibrational signatures of different molecules. Though used here to determine flow rates, this approach can also be employed in reverse for the characterization of an unknown diffusion coefficient if the flow rate is first established by following the mass transport of a species of known diffusion behavior.

References

1. A. J. de Mello, Nature **422**, 28 (2003).
2. S. Leung, R. F. Winkle, R. C. R. Wooton, and A. J. de Mello, Analyst (Cambridge, U.K.) **130**, 46 (2005).
3. D. E. Hertzog, X. Michalet, M. Jager, X. Kong, J. G. Santiago, S. Weiss, and O. Bakajin, Anal. Chem. **76**, 7169 (2004).
4. D. Pan, Z. Ganim, J. Kim, M. Verhoeven, J. Lugtenburg, and R. Mathies, J. Am. Chem. Soc. **124**, 4857 (2002).
5. P. Fletcher, S. Haswell, and X. Zhang, Electrophoresis **24**, 3239 (2003).
6. T. Araki, K. Ueno, H. Misawa, and N. Kitamura, Anal. Sci. **22**, 1283 (2006).
7. H. Wang, N. Bao, T. T. Le, C. Lu, and J. Cheng, Opt. Express **16**, 5782 (2008).
8. G. I. Petrov, R. Arora, A. Saha, R. D. Heathcote, S. Ravula, I. Brener, and V. V. Yakovlev, Proc. SPIE **6442**, 644209 (2007).
9. D. Schafer, J. A. Squier, J. van Maarseveen, D. Bonn, M. Bonn, and M. Müller, J. Am. Chem. Soc. **130**, 11592 (2008).
10. D. Sinton, Microfluid. Nanofluid. **1**, 2 (2004).
11. H. Kinoshita, S. Kaneda, T. Fujii, and M. Oshima, Lab Chip **7**, 338 (2007).
12. J. M. Chen, T. Horng, and W. Y. Tan, Microfluid. Nanofluid. **2**, 455 (2006).
13. R. F. Ismagilov, A. D. Stroock, P. J. A. Kenis, G. Whitesides, and H. A. Stone, Appl. Phys. Lett. **76**, 2376 (2000).
14. D. Schafer, E. A. Gibson, W. Amir, R. Erikson, J. Lawrence, T. Vestad, J. Squier, R. Jimenez, and D. W. M. Marr, Opt. Lett. **32**, 2568 (2007).
15. T. Park, M. Lee, J. Choo, Y. Kim, E. K. Lee, D. J. Kim, and S. Lee, Appl. Spectrosc. **58**, 1172 (2004).
16. J. Salmon, A. Ajdari, P. Tabeling, L. Servant, D. Talaga, and M. Joanicot, Appl. Phys. Lett. **86**, 094106 (2005).
17. S. K. Sia and G. M. Whitesides, Electrophoresis **24**, 3563 (2003).
18. H. A. Rinia, M. Bonn, and M. Müller, J. Phys. Chem. B **110**, 4472–4479 (2006).
19. E. M. Vartiainen, H. A. Rinia, M. Müller, and M. Bonn, Opt. Express **14**, 3622 (2006).

Fig. 3. (a) Sample data set showing the raw cars data: the quotient of the mCARS spectral intensity (I_{CARS}) with the background spectral intensity (I_{REF}) (upper curve) and the retrieved imaginary part of the third order susceptibility ($Im[X^{(3)}]$) (lower curve). (b) Strength of the ethanol resonance for five concentrations of ethanol in water: 20%, 14%, 10%, 6%, and 3%.